

A-train satellite observations of very little cloud invigoration by aerosols

Steven T. Massie, Leigh Munchak

National Center for Atmospheric Research, Boulder, Colorado, USA.

Jonathan H. Jiang, Hui Sui

Jet Propulsion Laboratory, California Institute of Technology, Pasadena, California, USA

Changes in occurrence-weighted and mass-weighted cloud heights are calculated as a function of aerosol optical depth (AOD) over the ocean and land in the tropics for 2008. The cloud height derivatives are calculated from an analysis of RL-GEOPROF cloud vertical structure data from the CALIPSO and CloudSat experiments. The structures are binned according to thermodynamic and dynamical influences (e.g. relative humidity from the AIRS experiment) and aerosol influences (i.e. MODIS AODs and MLS CO at 215 hpa, an aerosol proxy). Since not all cirrus in the upper troposphere is related directly to deep convection, the cloud structures are also binned according to the vertical depths of the observed cirrus, for cloud widths less than 1 km to those greater than 10 km. CloudSat data is used to specify the cloud mass densities associated with the cirrus of different vertical depths. Changes in RL-GEOPROF occurrence-weighted and mass-weighted centroids are less than 100 m per 0.1 increment change in AOD over the land and oceans for the annual average and seasons. The MLS derivatives do not indicate an increase in cloud heights as 215 hPa CO increases. These derivatives are substantially smaller (by factors between 2 and 10) than those calculated previously based upon MODIS cloud top pressure data.

1. Introduction

Aerosol-indirect effects are thought to have many diverse effects upon atmospheric physics [Lohmann and Feichter, 2005]. For a given amount of water vapor, an increase in aerosol number density will produce a larger number of smaller and more reflective cloud droplets [Twomey 1977], thus having a cooling effect on the atmosphere. Smaller cloud droplets collide less efficiently, prolonging droplet lifetimes [Albrecht 1989]. Aerosol may inhibit or enhance cloud dynamics. Absorptive aerosol can alter temperature profile stability, and inhibit cloud growth. An increase in aerosol concentrations is thought to suppress warm rain processes, permitting more liquid water to reach the homogeneous freezing level, and thereby enhance latent heat release in the upper portions of clouds [Khain et al., 2005; Rosenfeld et al., 2008]. This process is known as “cloud invigoration”. In general, uncertainties in the magnitude of aerosol-indirect effects are large, with uncertainties in radiative forcing (1760-present) near $1.5 \text{ W} / \text{m}^2$, a value as large as the positive forcing due to greenhouse gases [IPCC, 2008].

The potential for cloud invigoration to impact the radiative budget of the atmosphere, modulated by decadal trends in aerosol loading, is illustrated by considering the changes in the blackbody emission of optically thick clouds whose cloud tops increase in height by e.g. 0.1 and 1 km. The occurrence-weighted cloud heights discussed below are near 13 km. With a temperature lapse rate of $-7 \text{ K} / \text{km}$ near 13 km, the blackbody σT^4 emissions (with σ the Stefan-Boltzmann constant) associated with cloud tops near 13.1 and 14 km are 1.4 and $13.8 \text{ W} / \text{m}^2$ lower than that at 13 km. There are compensating considerations, however, since if increases in aerosol produce smaller ice particles, then clouds are more reflective at visible wavelengths, and cloud coverage likely also changes.

Cloud invigoration has recently been quantified by *Koren et al.* [2010a]. MODIS cloud top pressure and aerosol optical depth (AOD) data over the inter-tropical convergence zone in the tropical Atlantic (0 – 10 N, 20 -30 W) for July and August 2007 were binned for three AOD bins: $0 < \text{AOD} < 0.15$, $0.15 < \text{AOD} < 0.35$, and $0.35 < \text{AOD} < 1$. Data were subsetted into several categories, i.e. all data for all cloud top pressures, data with cloud fractions less than 20%, high cloud data (with cloud top pressures less than 600 hPa), and high clouds for cloud fractions less than 20%. Most of the MODIS data had cloud tops in the 600 to 1000 hPa range. Figures 5e and 6e of *Koren et al.* [2010a] display variations of cloud top pressures as a function of AOD for all data and the high cloud cases. The increase in cloud top pressure in their Figure 5e corresponds to an increase in cloud top height of 260 m and 120 m per 0.1 increment in AOD, for the all data and 20% cloud screened data cases, respectively. The increase in cloud top pressure in their Figure 6e corresponds to an increase in cloud top height of 170 m per 0.1 increment change in AOD for the high cloud data.

In a related paper, *Koren et al.* [2010b] calculate changes in cloud anvil heights as a function of MODIS AODs over the Atlantic (0 N to 14 N, 18 W to 45 W) and Pacific (0 N to 14 N, 180 W to 150 W) during June-July-August 2007. From Figure 3 of *Koren et al.* [2010b], anvil heights increase by approximately 430 and 880 m per 0.1 increment change in AOD over the Atlantic and Pacific, respectively. The anvil heights are between 11.1 and 11.7 over the Atlantic, and 11.9 and 13.2 km over the Pacific. If MODIS AOD data from adjacent grid boxes are used, the derivatives (see Figure 6 of *Koren et al.* [2010b]) are 666 and 987 m per 0.1 increment change in AOD over the Atlantic and Pacific. Finally, if the analysis is restricted to cases for which the mid-troposphere vertical velocity omega field is negative (i.e. cases of positive vertical velocity), based upon the NOAA-NCEP Global

Data Assimilation System fields, then the derivative over the Atlantic is 300 m per 0.1 increment change in AOD. In combination, the *Koren et al.* [2010a, 2010b] studies report a range of cloud invigoration between 170 and 987 m per 0.1 increment change in AOD.

It is well recognized that the quantification of aerosol-indirect effects is not an easy task. *Koren et al.* [2010a] and *Stevens and Feingold* [2009] discuss the difficulties inherent in using satellite data to quantify aerosol-cloud indirect effects. Measurements of aerosol optical depths in the vicinity of clouds are very difficult. Aerosol optical depths may change as a function of distance from clouds, due to changes in relative humidity (RH). A major challenge is to isolate changes in cloud properties, due to changes in aerosol, in a sea of meteorological variability.

Meteorological and cloud dynamic variability, however, is dependent upon many variables. Parcel buoyancy increases as the difference between the parcel and ambient air temperature increases, and decreases if water condensate is present in the parcel [*Rogers and Yau*, 1989]. Buoyancy decreases when ambient air is “entrained” into a parcel since the ambient air is usually drier and cooler than that of the parcel. Latent heat is released if changes in phase from vapor to liquid, and liquid to ice, occur during ascent, thereby increasing the parcel temperature and buoyancy. “Cloud invigoration” is thought to occur when changes in aerosol loading alter the vertical profile of latent heat release.

Clouds are of course three dimensional time-dependent structures with complicated internal structure and velocity fields. Current cloud simulations have identified a variety of considerations which influence the time development of clouds. Variations in relative humidity near the surface are known to produce differences in cloud structure [*Fan et al.* 2007]. As relative humidity increases, cloud ice water content and the horizontal extent of cloud anvils increase. *Fan et al.* [2007] note that increases in relative humidity are

correlated with increases in temperature profile instability as represented by convective available potential energy (CAPE, J / kg). Moisture values in low and middle troposphere altitudes are identified by *Sherwood* [1999] as a dominant factor, and CAPE values a minor factor, in the outbreak of convection in the tropical western Pacific area. This finding is supported by parcel model calculations of *Brown and Zhang* [1997] who note that parcel buoyancy is depleted by entrainment when parcels encounter dry air above the boundary layer. Cloud-resolving simulations by *Takemi et al.* [2004] also support this viewpoint. *Koren et al.* [2010a] note that the analyses fields of relative humidity and vertical pressure velocity are the two fields, out of numerous analyses fields, that are the most highly correlated with observed cloud top pressure values.

Fan et al. [2009] note that horizontal wind shear has an important effect upon cloud development. With strong wind shear, the increase in evaporative cooling in an isolated deep convective cloud is larger than the increase in condensational heating with increasing aerosols, leading to the suppression of convection. The presence of wind shear may also enhance the development, strength, and longevity of squall lines [*Weisman and Rotunno*, 2004], when the wind shear is aligned perpendicular to the squall line. Thus, specific spatial and temporal details of meteorological variations may either have a positive or negative effect on cloud development.

The temporal and scale dependent nature of cloud development is illustrated by the high resolution (100 m by 100 m in the horizontal and vertical) three dimensional simulation of shallow-to-deep convection over the Amazon of *Khairoutdinov and Randall* [2006]. Though sufficient CAPE is present during the start of the simulation, only shallow convection is present for several hours, with eddies not growing larger than 1 km in size. The eddies then start to coagulate into larger structures aligned along the moving edges of

cold pools, created by downdrafts which are negatively buoyant, when rain evaporates above the convective boundary layer. The larger structures then evolve into deep convection.

In this paper we analyze CloudSat-CALIPSO data to quantify changes in cloud vertical structure as Moderate Resolution Imaging Spectrometer (MODIS) aerosol optical depths and CO mixing ratios at 215 hPa increase. Our analysis focuses upon cloud structure at altitudes above 10 km altitude in the tropics. Section 2 discusses the data in our analyses: CloudSat-CALIPSO cloud structure data, MODIS AODs, and MLS CO at 215 hPa (an aerosol proxy). Section 3 discusses our methodology. Equal consideration is given to meteorological and dynamical fields and aerosol-cloud interactions. The fields of relative humidity near the surface, and at 500 and 200 hPa, wind shear, CAPE, pressure tendency, and liquid water paths, from analyses and/or satellite observations are used in our calculations to represent several of the meteorological and dynamical influences discussed above. Section 4 presents the results of our calculations of the changes in occurrence-weighted and mass-weighted cloud heights due to aerosol and meteorological influences. Section 5 presents our conclusions.

2. Data

Merged radar-lidar geospatial profile (RL-GEOPROF) data [Mace *et al.* 2009] specifies the upper and lower altitudes of cloud layers as jointly observed by the CloudSat and Cloud-Aerosol Lidar and Infrared Pathfinder Satellite Observations (CALIPSO) experiments. We analyze RL-GEOPROF data, available from <http://www.cloudsat.cira.colostate.edu/>, for 2008 for tropical latitudes between 20 S – 20 N. The CloudSat and CALIPSO experiments fly within 15 s of each other in the NASA A-train satellite constellation with observation times at 1330 and 0130 local

time [L'Ecuyer and Jiang, 2010]. CloudSat carries the first W-band (94 GHz) cloud profiling radar [Stephens *et al.* 2008]. CloudSat is unique in its ability to observe both cloud and precipitation. The CALIPSO experiment includes the CALIOP polarization lidar that observes at 532 and 1064 nm [Winker, Hunt, and McGill 2007]. Vertical resolution volumes for CloudSat and CALIPSO are 480 m and 60 m, respectively. Most of the cloud structure in the RL-GEOPROF data above 10 km is contributed by the CALIPSO experiment. We bin RL-GEOPROF data in 0.1 km altitude increments.

The satellite observation times, however, are not coincident with the diurnal convection maxima at 0500 over the tropical oceans and 1700 over the continents [Liu *et al.* 2008, Mace *et al.* 2009]. Ideally, it would be best to be able to observe the cloud tops when the storm activity is at its temporal and spatial peak. Figure 1 of Liu *et al.* [2008] presents frequency-by-altitude diagrams of Tropical Rainfall Measuring Mission Precipitation Radar (TRMM PR) reflectivity greater than 20 dBz over 20 S – 20 N over land and ocean. Reflectivity frequencies are contoured for frequency ranges from 0.9 to 14 % over the land and 2.3 to 7% over the ocean, with the 5% threshold indicating the presence of significant reflectivity. The reflectivity frequencies at altitudes greater than 10 km are greater than 5% over land between 13 – 21 hours, and over the ocean between 22 – 24 and 0 – 8 hours local time. The afternoon A-train observation time of 1330 is at the edge of the 5% frequency threshold over land, while the post-midnight 0130 time occurs when the frequencies over the ocean are greater than or equal to the 5% threshold.

Since mass-weighted cloud heights are discussed in this paper, CloudSat ice and liquid water content data (available from http://www.cloudsat.cira.colostate.edu/data_dist/OrderData.php) are processed to determine the annual-averaged cloud mass field for 2008 for 20 S to 20 N. The 2B-CWC-RO data files (with RO standing for radar only) contain liquid and ice contents (mg / m^3)

in an altitude grid with vertical spacing of 0.24 km. Ice water content (IWC) bias errors are estimated to be less than 40% [Austin *et al.*, 2009]. Differences in the IWC probability distribution functions (PDFs) of CloudSat and the Microwave Limb Sounder (MLS) are generally less than 50% [Wu *et al.*, 2008].

The MODIS experiment uses 36 visible and infrared spectral bands [King *et al.*, 1992, King *et al.*, 1999]. MODIS measures many parameters (e.g. cloud top temperature and pressure, cloud water and ice paths, cloud coverage fractions, aerosol AODs). We note that MODIS cloud top altitudes for optically thick clouds are approximately 1.5 km lower than CALIPSO cloud top altitudes [Minnis *et al.*, 2008] due to differences in visible-lidar and MODIS infrared radiative transfer considerations. The MODIS experiments began operation in February 2000 and July 2002 on the Terra and Aqua satellite platforms. Aerosol optical depths at 0.55 μm are retrieved over land [Kaufman *et al.*, 1997] and ocean [Remer *et al.*, 2002, Martins *et al.*, 2002] using different algorithms. Validation of MODIS AODs is discussed by Remer *et al.* [2005] for observations over the ocean, and Chu *et al.* [2002, 2003] over land. Aqua AODs, (available at <http://ladsweb.nascom.nasa.gov/data/>) are analyzed in this paper since the Aqua satellite is in the A-train. We subset our analyses over land and ocean due to the differences in the aerosol retrieval algorithms and due to the inherent differences between cloud temporal variations and cloud dynamics over land and ocean.

We use MODIS liquid water paths in our analyses as a proxy for water loading influences that are present in parcels. As discussed above in the Introduction, water loading will decrease parcel buoyancy. The validation of the MODIS water paths is discussed in Horvath *et al.* [2007]. MODIS and Tropical Rainfall Measurement Mission (TRMM) Microwave Imager (TMI) liquid water path means agree to 5 to 10% with an overall correlation coefficient of 0.85 for warm, non-precipitating clouds.

Atmospheric Infrared Sounder (AIRS) relative humidity profile data are used in our calculations to account for dynamical variations, following the discussion of [Fan *et al.* 2007]. The quality of the AIRS relative humidity and water vapor data is discussed by Gettelman *et al.* [2004] and Gettelman *et al.* [2006]. AIRS relative humidity (with respect to ice) values are reported when the cloud fraction is less than 70%. Water vapor and relative humidity measurements agree with aircraft measurements to within 25% and 9% at pressures less than 150 and 250 hPa, respectively. AIRS relative humidity values have an estimated dry bias of 4%. The AIRS level 3 (AIRS3STD) data is available at the NASA Goddard DAC at <http://mirador.gsfc.nasa.gov/cgi-bin/mirador/presentNavigation.pl?tree=project>. Relative humidity near the surface at 925 hPa, 500 hPa (near 5 km altitude), and at 200 hPa (near 11 km) are included in our analysis.

We also use the AIRS relative humidity data to calculate “vapor deficits”. Redelsperger *et al.* [2002] note that CAPE was not well correlated to cloud heights, observed during the Tropical Ocean Global Atmosphere Coupled Ocean-Atmosphere Response Experiment (TOGA COARE) in November of 1992. Instead, the “vapor deficit”, the differences of saturated specific humidity and moist specific humidity, averaged over the altitude range from 3 to 4.5 km altitude, is inversely correlated with cloud top heights. Smaller vapor deficits are associated with higher cloud tops heights. We use the AIRS data to calculate vapor deficits for AIRS pressures between 500 and 700 hPa.

Since aerosol is difficult to measure in the presence of clouds, we also analyze MLS CO at 215 hPa. MLS CO is retrieved from the 230 GHz CO emission line. MLS measurements of CO are influenced much less by the presence of clouds in the microwave, compared to measurements of MODIS AODs in the visible, since the ratios of cloud particle size to the microwave observation wavelength are much smaller than the

corresponding ratios of the MODIS measurements. Though the V2.2 data (available from <http://mirador.gsfc.nasa.gov/cgi-bin/mirador/presentNavigation.pl?tree=project>) is known to be large by a factor of two [Livesey *et al.* 2008], and is retrieved with a vertical resolution of 5 km, we are interested in relative changes in cloud altitude structure as CO changes. We bin the CO data into three bins (e.g. 100-150, 150 – 200, 200-250 ppbv at 215 hPa). As presented in Figure 1 of Jiang *et al.* [2008], MODIS AODs and MLS CO measurements at 215 hPa are correlated above the Amazon, especially during the dry season, and less so during the wet season, since rainfall processes washout aerosols. Jiang *et al.* [2009] presents MODIS AOD versus MLS CO relationships for other regions of the world on a month by month basis.

We use various fields from the National Centers for Environmental (NCEP) Final Global Data Assimilation System (FNL), which is the final run of the Global Forecast System model with assimilated observations. Analyses are provided on a 1° by 1° global grid every 6 hours at 21 pressure levels from 1000 to 100 hPa. Values of maximum CAPE during the day, the maximum wind shear (m / s) between ground and 7 km (i.e. 253 hPa), and the vertical pressure velocity (omega, Pa / s) at 500 hPa are incorporated into our analyses.

3. Methodology

RL-GEOPROF data files for 2008 are processed in the following manner. For each day, the cloud structure in each 1° x 1° latitude-longitude grid cell is determined in an altitude profile between ground level and 20 km, with a 0.1 km vertical resolution, based upon the layer structures specified in the RL-GEOPROF data files. A single observation profile may have more than one cloud layer. Counts of unity are registered for all altitude levels between the cloud top

and cloud bottom of each cloud layer. The counting is binned according to the depth of the cloud layer, with binning for depth ranges 0.1-1, 1-2, 2-3, 3-4, 4-10, and 10-20 km.

MODIS AODs and water paths, and AIRS relative humidity fields are first averaged into a uniform $1^\circ \times 1^\circ$ latitude-longitude grid so that daily AODs can be easily related to the daily RL-GEOPROF cloud structure and NCEP FNL data files. Using the NCEP FNL data and the MODIS AODs, processing bins cloud counts as a function of altitude z , cloud depth D , AIRS relative humidity RH , and AOD. Binning is performed in increments of 10% relative humidity, from 0 to 100%, and increments of 0.1 AOD from 0.1 to unity.

Since MODIS observations of aerosol are difficult in the presence of clouds, MODIS AODs are also averaged over $3^\circ \times 3^\circ$, and are matched with the CloudSat $1^\circ \times 1^\circ$ latitude-longitude grid cells. This reduces the noise of the MODIS AODs, and increases the number of data points that can be used in our calculations. Over the land (ocean), the fraction of positive MODIS AODs increases from 64 % (53%) to 90 % (87%). For AODs less than 0.4 (the upper limit of AODs used in our study), the correlation coefficients of $1^\circ \times 1^\circ$ and $3^\circ \times 3^\circ$ AODs are 0.84 and 0.91. A least squares linear fit to these individual data points indicates that the $1^\circ \times 1^\circ$ AODs are higher than the $3^\circ \times 3^\circ$ AODs by 0.051 and 0.027 over land and ocean, respectively. The use of $3^\circ \times 3^\circ$ AODs therefore increases sampling statistics and does not introduce prohibitive AOD biases.

The binning by cloud depth is necessary since subvisual cirrus is formed by in-situ processes and by blow-off by deep convection [Pfister *et al.*, 2001]. The in-situ processes, by which humid air layers slowly rise near the tropopause and form layers of small vertical depth, are not necessarily directly related to deep convection. Pfister *et al.* [2001] used back trajectory analysis to relate thin and thicker cirrus (depths of several km) to deep convection. The thicker cloud structures were related to outflow from convection 0.5 to 3 days downwind of convection.

Massie et al. [2002] used back trajectory calculations in an analysis of Halogen Occultation Experiment (HALOE) cirrus extinction data and concluded that half of the HALOE cirrus observations over the maritime continent were consistent with the convective blow-off formation process, while the other half were consistent with in situ formation processes. The depth binning therefore allows us to calculate vertical displacements of cloud structure with and without small depth cirrus (i.e. cirrus not related to convective activity).

Since the number of AOD observations decreases as AOD increases, it is useful to use normalized cloud structure curves. For a given number of cloud counts $N(z, D)$ between altitude z and $z + 0.1$ km for cloud depth D , the normalized cloud structure curve $A(z, D, RH, AOD)$ is

$$A(z, D, RH, AOD) = N(z, D, RH, AOD) / \sum N(z, D, RH, AOD) \quad (1)$$

with the summation in the denominator over all altitude bins.

The question then arises as to how to measure the appropriate changes in cloud heights due to invigoration processes. There is a range of observed cloud top heights and cloud depths. The calculation of an altitude weighted centroid that integrates over a range of altitude is therefore appropriate. Since the cloud invigoration process implies an increase in imparted energy release in the cloud development process, the calculation of a mass and altitude weighted centroid also is appropriate.

The Z_C centroid of cloud occurrence is calculated from the expression

$$Z_C = \int A z dz / \int A dz \quad (2)$$

with limits of integration between 10 and 17 km altitude. We focus on that portion of the troposphere for which cirrus is prevalent. The Z_M mass weighted centroid is calculated from the expression

$$Z_M = \int A \rho z dz / \int A \rho dz \quad (3)$$

again with limits of integration between 10 and 17 km altitude, and where $\rho(z, D)$ is the CloudSat ice content. The mass density is a function of the cloud depth D since cirrus of small vertical depth has a mass density substantially less than cirrus of extensive vertical depth. The normalized curves A are useful for graphical purposes in that A curves of different D , RH , and AOD values have similar ranges of the A values. Note that use of N or A in equation (2) yields the same Z_C values since the denominator of equation (1) is altitude independent. This also applies to the Z_M value of equation (3).

If cloud invigoration is present, then Z_C and Z_M values will increase as AODs (and CO mixing ratios at 215 hPa) increase. Calculations of Z_C and Z_M values are presented below in Section 4 for cases in which all cloud depths are used, and for which cirrus of small vertical depth D are excluded (i.e. only cloud depths greater than 1 or 2 km are used). The subsetting for depths greater than 1 and 2 km follows from previous studies of the vertical distributions of cirrus near the tropopause. Figure 12 of *Massie et al.* [2010] presents CALIPSO vertical cloud depth probability distribution functions (pdfs) at 16, 17, and 18 km altitude. The pdfs peak between 0.8 and 1.0 km vertical depth, while 2 km vertical depths are located in the tails of the pdfs.

Though the data is gridded at an altitude increment of 100 m, and the Calipso data has a vertical resolution of 60 m, equation (3) centroids can be calculated with accuracy better than 100 m. We calculated Z_c centroids of $A(z)$ curves two ways. We first fit a representative annual $A(z)$ curve with a high-order polynomial. We determined that the rms differences of $A(z)$ and the polynomial fit was on the order of 2% (i.e. that the $A(z)$ curve had a 2% noise structure). Our first case calculation calculated the Z_c centroid at a vertical resolution of 10 m, integrating over the 10 to 17 km range, using the polynomial fit to $A(z)$ with no perturbations of $A(z)$. Our second case calculation calculated several hundred Z_c centroids at a vertical resolution of 100 m, using

the polynomial fit, modified by random perturbations of $A(z)$ of 2%. The average centroid from these perturbed calculations differed from the precise calculation by 30 m.

4. Results

Figure 1 presents two panels of normalized cloud counts over the Tropics (20S – 20N) over land in 2008 for all months of the year and three bins of MODIS AODs (0.10 – 0.20, 0.20-0.30, 0.30-0.40), for two AIRS relative humidity bins of 60-70% and 80 – 90% at 925 hPa. We subset our calculations of the altitude centroids and their derivatives using three relative humidity bins (i.e. 60-70%, 70-80%, and 80-90% at 925 hPa) in order to isolate aerosol effects from dynamics and to look for consistency amongst the derivatives calculated for each relative humidity bin. The data points in Figure 1 are calculated and presented in 0.1 km altitude steps. All cloud depths are utilized in the curves presented in Figure 1. All curves have largest cloud occurrences of deep convection at altitudes above 10 km, and large occurrences of shallow clouds near the surface at altitudes below 3 km. Figure 1 curves were calculated for AODs using MODIS $1^\circ \times 1^\circ$ latitude-longitude grid cells that are spatially matched with CloudSat $1^\circ \times 1^\circ$ latitude-longitude grid cells. The number of observations that are associated with each point of each normalized curve is on the order of 10^4 . Curves for which MODIS satellite averages over $3^\circ \times 3^\circ$ longitude grid cells are very similar (not shown), and have less noise than the $1^\circ \times 1^\circ$ curves due to the increased number of cloud counts at each altitude.

The variations in the normalized counts near 13 km altitude in Figure 1 are due to variations in relative humidity at 200 hPa. Figure 2 presents normalized curves with specifics similar to Figure 1, except that AIRS relative humidity data is selected to vary between 60 and 90% at 200 hPa. The separation in the peak A values near 13 km is less than those in Figure 1, especially for

the 0.1 and 0.2 AOD curves. Figure 2 indicates that as one limits the ranges of the meteorological and dynamical variables that can influence the shape of the A curve, in both the lower and upper troposphere, that the differences in the A curves become smaller for curves of different AOD. Equations (2) and (3) are applied with and without consideration of the relative humidity at 200 hPa.

Figure 3 displays variations in the cloud occurrence centroids over land for 20 S to 20 N for cases in which a) all cloud depths are incorporated into equation (2) and when b) the centroid integrals only include cloud depths greater than 2 km. Centroids increase by 20 and 58 m per 0.1 increase in AOD for the two cases, respectively, for the $1^\circ \times 1^\circ$ AODs. These average derivatives are calculated by first determining three Z_c derivatives for each of the three relative humidity ranges at 925 hPa, using Z_c values at AODs of 0.1 and 0.3, followed by an averaging of the three derivatives. It is expected that the derivatives will be smaller for case a) since this case includes cirrus which is not directly related to convection, and is more attributable to local in-situ (height insensitive) physics in the upper troposphere.

Figure 4 displays variations in the mass centroids over land for 20 S to 20 N for cases in which all cloud depths are incorporated into equation (3) and when the integrals only include cloud depths greater than 2 km. Centroids increase by 36 and 26 m per 0.1 increase in AOD for the $1^\circ \times 1^\circ$ AODs for the all cloud depths and cloud depths greater than 2 km cases, respectively. The average derivatives for each case are calculated by determining the three derivatives of Z_m at 0.1 and 0.3 AOD for each of the three relative humidity ranges at 925 hPa, followed by an averaging of the three derivatives.

These derivatives, and others, are presented in Table 1. The 1° and 3° derivatives are fairly similar for the land observations, while the 3° Z_c derivatives are smaller than the 1° ocean

derivatives. Since half of the subvisual cirrus is likely directly related to deep convection, the derivatives for cirrus depths greater than 2 km are an appropriate measure of cloud invigoration. The Table 1 values indicate that cloud invigoration enhances cloud centroids, and mass weighted centroids, by less than 60 m per 0.1 AOD increment change over land, and less than 90 m per 0.1 AOD over the ocean. These derivatives are substantially less than the 170 m to 987 per 0.1 AOD increment changes calculated by *Koren et al.* [2010a] and *Koren et al.* [2010b].

Table 2 presents derivatives using 3° AODs, and in which relative humidity is restricted to the 60 to 90% range at 200 hPa. The derivatives using 1° AODs are not presented because the A curves (not shown) are noticeably noisy, especially over the ocean, due to a smaller number of observation points. The Table 1 values indicate derivatives less than 80 m per 0.1 AOD increment for the Z_c and Z_m centroids.

One can argue, however, that the use of the Table 2 derivatives may be unwise. First of all, there is a smaller total number of data points that are used to calculate the Table 2 derivatives. Smaller sampling introduces the likelihood that the sampling of the complete ranges of all variables, including dynamical influences, becomes less likely. A second point is that cloud invigoration is expected to be initiated mostly near cloud base. This is the crucial altitude range for which the dynamical influences (such as relative humidity) need to be accounted for. The Table 1 derivatives are therefore sufficiently appropriate. Our discussion of results will however look at calculations in which relative humidity at 200 hPa is constrained to a specific range of relative humidity.

By subsetting the calculations to the four seasons, we note that altitude Z_c centroids differ from season to season (see Table 3). The “Original” columns correspond to derivative data similar to that in Figures 3 and 4, in that only the AOD and RH dependencies of the Z_c and Z_m centroids are used to calculate the derivatives. The “Corrected” column incorporates additional

meteorological variables, and is discussed below. The largest “Original” derivatives are for June-July-August (JJA), with values near 169 and 110 m per 0.1 AOD increment over land and ocean, respectively. These values are similar to that of the increase in cloud top height of 170 m per 0.1 increment change in AOD for the MODIS high cloud data over the ocean as analyzed by *Koren et al.* [2010a] for JJA.

While binning by relative humidity at 925 hPa removes some of the variability due to dynamics, it does not capture all of the variability due to changes in the dynamics. This is apparent from examination of Figure 5, in which correlations of MODIS AODs over the land and tropics (20 S – 20 N) for RH between 70 and 80 % at 925 hPa are correlated with the mean values of AIRS RH at 500 hPa, MODIS water paths (g/m^2), vapor deficits (g/kg), NCEP FNL CAPE (J/kg), vertical wind shear (U_{shear}) of the horizontal wind (m/sec), and omega (pressure tendency at 500 hPa) (hPa/sec) values in JJA of 2008 for cloud depths greater than 2 km. The calculation of wind shear follows the work of *Fan et al.* [2009], in that U_{shear} is specified by subtracting the maximum and minimum U values between ground level and 7 km altitude.

Relative humidity at 500 hPa increases in Figure 5 as AOD increases. This implies that dryer air is likely encountered by parcels at the lower AOD values, which will decrease the buoyancy of rising air parcels. Water paths decrease as AODs increase. Again the parcels at lower AODs will have more water loading and a decrease in buoyancy relative to higher AOD parcels. Vapor deficits decrease with increases in AODs. Average CAPE, which is of moderate magnitude, increases as the AODs increase over land and ocean. Wind shear decreases over the land, and omega decreases (i.e. the vertical velocity becomes less negative) over land and ocean, as AODs increase. The panels in Figure 5 generally indicate that dynamical parameters change such that dynamical influences consistently enhance parcel buoyancy and cloud heights as AODs increase

in JJA. The upward trends in the centroids presented in Figures 3 and 4 undoubtedly are influenced by meteorological and cloud dynamical factors.

We note that the dependencies present in Figure 5 for JJA are not as strong in other graphs for the other seasons (not shown). CAPE over land for the other seasons does not increase by more than 150 J / kg as AODs increase, while CAPE changes by 500 J / kg during JJA as AODs increase. Water paths over land decrease by 20 g / m² in JJA as AODs increase, and by half that amount in September – November and December – February. RH at 500 hPa over land increases by 20% in JJA as AODs increase, and half that amount for the other seasons. The variations of the means in Figure 5 are reflective of sampling differences. There is not a good reason to suspect that e.g. larger water paths are always associated with larger AODs. The vertical bars associated with each symbol in Figure 5 are the 95% confidence limits of the determination of the mean values. Since the vertical lines along an individual land or ocean curve do not overlap, the differences in the mean values are meaningful. The standard deviations, however, are large and are on the order of the mean values themselves. The differences in the means in Figure 5 indicate small differences that are present in wide distributions.

The ramifications of the dynamical dependencies for JJA in Figure 5 are apparent by examining how correlations of AOD with the dynamical variables might possibly impact the calculations of the centroid derivatives. We start with the following equation for the altitude centroid Z_c

$$Z_c = \text{const} + \sum \{ (V(i) - V_{\text{ref}}(i)) \partial Z_c / \partial V(i) \} \quad (4)$$

where the i summation is over the variable set {AOD, RH at 925 hPa, omega, CAPE, RH at 500 hPa, water paths, wind shear}, and where V_{ref} are reference (representative) values of the variables. This variable set is selected in order to represent the influence of AODs upon cloud heights, the positive meteorological influences of RH near the surface, omega, and CAPE, and

the negative influences of RH at 500 hPa, condensate burdens, and wind shear, which were discussed in the Introduction. Equation (4) equation is adopted from equation 8.8 of *Stevens and Brenguier* [2009], who point out that it is the accuracy of the sum of the products $\{ (V(i) - V_{\text{ref}}(i)) \partial Z_c / \partial V(i) \}$ of the dynamical variables, and not the differences $(V(i) - V_{\text{ref}}(i))$, which limit one's ability to disentangle meteorological effects from aerosol effects.

Several papers provide some guidance as to the size of the derivatives. Figure 2 of *Jensen and Del Genio* [2006] presents “a hint of a relationship between increasing low-level CAPE, and increasing convective cloud-top height”. Using the means of the cloud top heights of cumulus congestus clouds from their Figure 2, cloud top heights increase in the 5 to 8 km altitude range by approximately 1 m / (J / kg). In contrast, Figure 12 of *Redelsperger et al.* [2002] indicates that clouds less than 6 km in height do not increase in height as CAPE increases. Their Figure 16 indicates that cloud heights do increase sharply as vapor deficits decrease to values less than 2.5 g kg⁻¹, and less so for vapor deficits between 2.5 and 4 g kg⁻¹. Using their data at 5 and 2.5 km, the cloud heights change by 1.8 km / (g / kg). *Sherwood et al.* [2004] indicate that a 20% decrease in humidity above the boundary layer, for pressures between 500 and 750 hPa, over Florida and Key West during the CRYSTAL-FACE field study lead to a 1 km decrease in cloud heights. This translates to a derivative of -50 m / % RH. Figure 6 of *Khain et al.* [2005] presents calculations of maximum cloud top heights versus accumulated rain amounts for cases with and without wind shear. The cloud heights for the representative accumulated rain amount of 0.4 mm change by - 108 m / (m / sec). *Fan et al.* [2009] consider wind shears greater than 10 m/sec within 7 km of the ground level to be strong. We note from our Figure 5 in JJA that strong wind shear is present at an AOD of 0.1 in JJA. Tables 2 and 3 of *Fan et al.* [2009] indicates that maximum updraft velocities and averaged latent heat release rates decrease as the cloud

condensation nuclei increase for the strong wind shear cases. They also note that the decreasing rate of updrafts is greater for humid air than for drier air.

We calculated $\partial Z_c / \partial V(i)$ derivatives by applying the IDL “Regress” linear regression routine. Inputs to the calculation included Z_c centroids and the means of the set {AOD, RH at 925 hPa, omega, CAPE, RH at 500 hPa, water paths, wind shear} calculated for each season. The Regress routine was applied with each data point given a Gaussian weight equal to the inverse of the variance of the Z_c values, or these values scaled by a constant. All calculations produced a reduced χ^2 of unity, which is important for the comparisons of the derivative to its 2σ uncertainty. The most significant (2σ) derivative is that of the cloud water path, with a value of $-3.6 \text{ m} / (\text{g} / \text{m}^2)$. By sub-sampling the data for low and high shear cases, and restricting the calculation to water paths between 110 and 130 g / kg , the 2σ derivative of CAPE is $0.5 \text{ m} / (\text{J} / \text{kg})$ and the (1σ) derivative due to wind shear is $-7 \text{ m} / (\text{m} / \text{sec})$. The CAPE derivative is half as large of that estimated using Figure 2 of *Jensen and Del Genio* [2006], and the shear derivative is over ten times smaller than that estimated from Figure 6 of the *Khain et al.* [2005] cloud simulation.

We note that the graph of the cloud centroids versus the wind shear (not shown) is suggestive of non-linearity. The centroids decrease in value for wind shears greater than $10 \text{ m} / \text{sec}$, with a gradient near $-80 \text{ m} / (\text{m} / \text{sec})$, in line with the simulations of *Fan et al.* [2009]. The centroids increase in value for shears less than $5 \text{ m} / \text{sec}$, with a derivative near $20 \text{ m} / (\text{m} / \text{sec})$. Situations with very low wind shear are known to inhibit cloud development since falling rain will decrease buoyancy.

To illustrate the influence of the meteorological variables, the water path derivative of $-3.6 \text{ m} / (\text{g} / \text{m}^2)$, a CAPE derivative of $0.5 \text{ m} / (\text{J} / \text{kg})$, and a wind shear derivative of $-7 \text{ m} / (\text{m} / \text{sec})$ was used to calculate $\{ (V(i) - V_{\text{ref}}(i)) \partial Z_c / \partial V(i) \}$ corrections for each season. These

corrections were subtracted from the Original Z_c values, followed by new determinations of $\partial Z_c / \partial \text{AOD}$ derivatives using the corrected Z_c values at 0.1 and 0.3 AOD. These derivatives are labeled “Corrected” in Table 3. The corrections take the “Original” derivatives in JJA of 169 and 110 over land and ocean, respectively, to “Corrected” values of 58 and 51 m per 0.1 AOD increment. Most of the correction is due to the water paths, indicating the importance of water loading. The corrections for the other seasons use the same derivatives and are substantially less in magnitude. Though the estimation of the derivatives is admittedly difficult due to the scatter in the data, this calculation points out that dynamical and meteorological corrections are likely very important, and that exclusion of these terms, in the presence of correlations of the dynamical variables with AOD (see Figure 5), produces $\partial Z_c / \partial \text{AOD}$ derivatives that are too large.

Finally, since aerosol is difficult to measure in the vicinity of clouds, MLS CO at 215 hPa was also used to quantify cloud invigoration. Figure 6 displays normalized cloud structure curves over the tropics and land in 2008 for all months for three CO ranges (100 – 150, 150 - 200, and 200 – 250 ppbv) for cloud depths greater than 2 km. The cloud ice water contents (IWC), i.e. the $\rho(z,D)$ values, are greater than $3.5 \text{ mg} / \text{m}^3$ for cloud depths greater than 2 km at altitudes near 13.5 km, corresponding to pressures near 147 hPa. *Jiang et al.* [2007] indicates in their Figure 4 that MLS IWCs greater than $3 \text{ mg} / \text{m}^3$ at 147 hPa, accompanied by large surface CO emissions, correspond to a regime of strong convection and surface emissions. Our application of equations (2) and (3) for cloud depths greater than 2 km therefore applies an IWC screening similar to that discussed by *Jiang et al.* [2007]. The three CO ranges specified above also approximately correspond to the three aerosol ranges of Figures 1 – 5. Similar to Figures 1 and 2, cloud occurrence maxima are present in Figure 6 between 13 and 14 km altitude, and at altitudes near 3

km. Cloud occurrence and mass centroids are presented in Figure 7. Cloud invigoration (i.e. increases in Z_C and Z_M values as CO increases at 215 hPa) is not apparent in Figure 7.

5. Conclusions

The CloudSat-CALIPSO RL-GEOPROF data for cirrus at altitudes greater than 10 km has derivatives of occurrence-weighted and mass-weighted cloud heights for the annual average and seasons (excluding JJA) of less than 100 m per 0.1 increment change in AOD over land and ocean, respectively, for 2008. These derivatives are substantially smaller (by factors between 2 and 10) than those calculated previously based upon the MODIS cloud top pressure data for JJA. *Koren et al.* [2010a] calculated that MODIS cloud top pressures decreased with an increase in MODIS AOD. In terms of altitude, cloud top heights increased by 170 m per 0.1 increment change in AOD for clouds with pressures less than 600 hPa. *Koren et al.* [2010b] calculated that MODIS cloud top anvil heights increased by between 300 and 987 m per 0.1 increment in AOD over the Atlantic and Pacific during JJA 2007.

Our calculations were based upon a subsetting of the data according to both dynamical and microphysical variables, and also according to the vertical depth of the cirrus, since approximately half of the subvisual cirrus of small vertical depth is formed in-situ. Following the work of *Koren et al.* [2010a] and *Fan et al.* [2007], relative humidity is a key dynamical variable, and subsetting according to relative humidity is mandatory. The key microphysical variables in our study are AODs and CO (an aerosol proxy). Derivatives using MODIS AODs are small (see Figures 3 and 4, and Tables 1-3) even if one only considers two variables (i.e. AODs and AIRS RH at 925 hPa). The derivatives decrease when additional meteorological variables are considered. This is evident when one looks at the results of our regression analysis whereby aerosol, meteorological, and cloud dynamical variables are placed upon an equal

consideration. The small influence of cloud invigoration is apparent if one uses either MODIS AODs or MLS CO values at 215 hPa.

Though the derivatives $\partial Z_c / \partial V(i)$ for the dynamical variables are difficult to estimate, our analyses indicates that dynamical influences are very likely to be important. From a qualitative perspective, RH at 500 hPa and CAPE increases, and water paths, vapor deficits, wind shear, and omega decreases over land and ocean, as AODs increase in JJA (see Figure 5). The derivatives in JJA are larger than those in other seasons (see the “Original” column derivatives in Table 3). Our regression analyses suggests that variations in water path are influential in modulating cloud top heights, with CAPE and wind shear influential to a smaller degree. This is consistent with the basic ideas discussed in the Introduction in regard to the variables and factors that influence parcel buoyancy, e.g. the negative effect upon buoyancy by water loading. This has the important ramification that dynamical and meteorological corrections are likely very important in determining the accuracy of the aerosol microphysical $\partial Z_c / \partial AOD$ derivatives, and that exclusion of these terms, in the presence of correlations of the dynamical and meteorological variables with AOD, produces $\partial Z_c / \partial AOD$ derivatives that are too large.

Future work will expand upon the calculations presented in this paper. Additional processing of the GFS analyses fields and AIRS relative humidity data is required to expand our analyses to other years. This will allow us to better determine the dynamical and meteorological variables and possibly focus upon smaller regions of the world (e.g. India, China, etc).

Determination of the centroid derivatives of the dynamical variables is an obvious important goal. Our literature search found little quantitative information on the dynamical and meteorological derivatives. Future calculations also will examine other aspects of aerosol-indirect physics. Changes in albedos (using CERES data), and cloud fractions (using OMI and

MODIS data), due to changes in MODIS AODs and MLS CO mixing ratios, will be studied using the framework discussed in this paper.

Acknowledgements

This research is supported by NASA grants NNX10AM24G and the ACMAP program. The work was conducted jointly at the National Center for Atmospheric Research (NCAR) and the Jet Propulsion Laboratory (JPL), California Institute of Technology (Caltech). NCAR is sponsored by the National Science Foundation. JPL/Caltech is sponsored by NASA. We acknowledge the helpful comments of Eric Jensen, Mary Barth, J. F. Lamarque, Wojciech Grabowski, and Hugh Morrison in the preparation of this paper.

References

- Austin, R. T., A. J. Heymsfield, and G. L. Stephens (2009), Retrieval of ice cloud microphysical parameters using the CloudSat millimeter-wave radar and temperature, *J. Geophys. Res.*, *114*, D00A23, doi:10.1029/2008JD010049.
- Brown, R. G., and C. Zhang (1997), variability of Midtropospheric Moisture and Its Effect on Cloud-Top Height Distribution during TOGA COARE, *J. Atmos. Sci.*, *54*, 2760-2774.
- Chu, D.A., et al. (2002), Validation of MODIS aerosol optical depth retrieval over land, *Geophys. Res. Lett.*, *29*, No. 12, 1617, 10.1029/2001GL013205.

566 Chu, D. A., Y. J. Kaufman, G. Zibordi, J-D Chern, J-M Mao, C. Li, and H. B. Holben (2003),
 567 Global Monitoring of Air Pollution over Land from EOS-Terra MODIS, *J. Geophys. Res.*,
 568 108(D21), 4661, doi: 10.1029/2002JD003179.
 569
 570 Fan, J., R. Zhang, G. Li, and W.-K. Tao (2007), Effects of aerosols and relative humidity on
 571 cumulus clouds, *J. Geophys. Res.*, *112*, D14204, doi:10.1029/2006JD008136.
 572
 573 Fan, J., T. Yuan, J. M. Comstock, S. Ghan, A. Khain, L. R. Leung, Z. Li, V. J. Martins, and M.
 574 Ovchinnikov (2009), Dominant role by vertical wind shear in regulating aerosol effects on deep
 575 convective clouds, *J. Geophys. Res.*, *114*, D22206, doi:10.1029/2009JD012352.
 576
 577 Gettelman, A., et al. (2004), Validation of Aqua satellite data in the upper troposphere and lower
 578 stratosphere with in situ aircraft instruments, *Geophys. Res. Lett.*, *31*, L22107,
 579 doi:10.1029/2004GL020730.
 580
 581 Gettelman, A., et al. (2006), Climatology of Upper-Tropospheric Relative Humidity from the
 582 Atmospheric Infrared Sounder and Implications for Climate, *J. Clim.*, *19*, 6104-6121.
 583
 584 Horva'th, A ´., and R. Davies (2007), Comparison of microwave and optical cloud water path
 585 estimates from TMI, MODIS, and MISR, *J. Geophys. Res.*, *112*, D01202,
 586 doi:10.1029/2006JD007101.
 587
 588 Jensen, M. P., and A. D. De; Genio (2006), Factors Limiting Convective Cloud-Top Height at
 589 the ARM Nauru Island Climate Research facility, *J. Clim.*, *19*, 2105-2117.

590

591 Jiang, J. H., N. J. Livesey, H. Su, L. Neary, J. C. McConnell, and N. A. D. Richards (2007),

592 Connecting surface emissions, convective uplifting, and long-range transport of carbon

593 monoxide in the upper troposphere: New observations from the Aura Microwave Limb Sounder,

594 *Geophys. Res. Lett.*, 34, L18812, doi:10.1029/2007GL030638.

595

596 Jiang, J. H., H. Su, M. R. Schoeberl, S. T. Massie, P. Colarco, S. Platnick, and N. J. Livesey

597 (2008), Clean and polluted clouds: Relationships among pollution, ice clouds, and precipitation

598 in South America, *Geophys. Res. Lett.*, 35, L14804, doi:10.1029/2008GL034631.

599

600 Jiang, J. H., H. Su, S. T. Massie, P. R. Colarco, M. R. Schoeberl, and S. Platnick (2009),

601 Aerosol-CO relationship and aerosol effect on ice cloud particle size: Analyses from Aura

602 Microwave Limb Sounder and Aqua Moderate Resolution Imaging Spectroradiometer

603 observations, *J. Geophys. Res.*, 114, D20207, doi:10.1029/2009JD012421.

604

605 Kaufman, Y. J., et al. (1997), Operational remote sensing of tropospheric aerosol over land from

606 EOS moderate resolution imaging spectroradiometer, *J. Geophys. Res.*, 102, No D14, 17051-

607 17067.

608

609 Khain. A., D. Rosenfeld, and A. Pokrovsky (2005), Aerosol impact on the dynamics and

610 microphysics of deep convective clouds, *Q. J. R. Meteorol. Soc.*, 131, 2639-2663,

611 doi:10.1256/qj.04.62.

612

613 Khairoutdinov, M., and D. Randall (2006), High-Resolution Simulation of Shallow-to-Deep
 614 Convection Transition over Land, *J. Atmos. Sci.*, 63, 3421-3436.
 615
 616 King, M. D., Y. J. Kaufman, W. P. Menzel, and D. Tanre (1992), Remote Sensing of Cloud,
 617 Aerosol, and Water vapor Properties from the Moderate Resolution Imaging Spectrometer
 618 (MODIS), *IEEE Trans. Geosci. Remote Sens.*, 30(1), 2-27.
 619
 620 King, M. D., Y. J. Kaufman, D. Tanre, and T. Nakajima (1999), Remote Sensing of Tropospheric
 621 fromSpace: Past, Present, and Future, *Bull. Am. Met. Soc.*, 80, 2229-2259.
 622
 623 Koren, I., G. Feingold, and L. A. Remer (2010a), The invigoration of deep convective clouds
 624 over the Atlantic: aerosol effect, meteorology or retrieval artifact? *Atmos. Chem. Phys.*, 10, 8855-
 625 8872.
 626
 627 Koren, I., L. A. Remer, O. Altaratz, J. V. Martins, and A. David (2010b), Aerosol-induced
 628 changes of convective cloud anvils produce strong climate warming. *Atmos. Chem. Phys.*, 10,
 629 5001-5010.
 630
 631 L'Ecuyer, T. S., and J. H. Jiang (2010), Touring the Atmosphere Aboard the A-train, *Physics*
 632 *Today*, July 2010, 36-41.
 633
 634 Liu, C., E. J. Zipser, G. G. Mace, and S. Benson (2008), Implications of the differences between
 635 daytime and nighttime CloudSat observations over the tropics, *J. Geophys. Res.*, 113, D00A04,
 636 doi:10.1029/2008JD009783.

637

638 Lohmann, U., and J. Feichter (2005), Global indirect aerosol effects: a review, *Atmos. Chem.*
639 *Phys.*, *5*, 715-737.

640

641 Livesey, N. J., et al. (2008), Validation of Aura Microwave Limb Sounder O₃ and CO
642 observations in the upper troposphere and lower stratosphere, *J. Geophys. Res.*, *113*, D15S02,
643 doi:10.1029/2007JD008805.

644

645 Mace, G. G., Q. Zhang, M. Vaughan, R. Marchand, G. Stephens, C. Trepte, and D. Winker
646 (2009), A description of hydrometeor layer occurrence statistics derived from the first year of
647 merged CloudSat and CALIPSO data, *J. Geophys. Res.*, *114*, D00A26,
648 doi:10.1029/2007JD009755.

649

650 Martins, J. V., et al. (2002), MODIS Cloud screening for remote sensing of aerosols over ocean
651 using spatial variability, *Geophys. Res. Lett.*, *29*, No. 12, 1619, 10.1029/2001GL013252.

652

653 Massie, S., A. Gettelman, W. Randel, and D. Baumgardner, Distribution of tropical cirrus in
654 relation to convection, *J. Geophys. Res.*, *107*(D21), 4591, doi:10.1029/2001JD001293, 2002.

655

656 Massie, S. T., J. Gille, C. Craig, R. Khosravi, J. Barnett, W. Read, and D. Winker (2010),
657 HIRDLS and CALIPSO observations of tropical cirrus, *J. Geophys. Res.*, *115*, D00H11,
658 doi:10.1029/2009JD012100.

659

Minnis, P., C. R. Yost, S. Sun-Mack, and Y. Cchen (2008), Estimating the top altitude of optically thick ice clouds from thermal infrared satellite observations using CALIPSO data, *Geophys. Res. Lett.*, 35, L12801, doi:10.1029/2008GL033947.

Pfister, L., et al., Aircraft observations of thin cirrus clouds near the tropical tropopause, *J. Geophys. Res.*, 106, 9765–9786, 2001.

Remer, L. A., Y.J. Kaufman, D. Tanré, S. Mattoo, D. A. Chu, J. V. Martins, R-R. Li, C. Ichoku, R. C. Levy, R.G. Kleidman, T. F. Eck, E. Vermote, and B. N. Holben (2005), The MODIS Aerosol Algorithm, Products and Validation, *J. Atmos. Sci.*, 62, 947-973.

Rogers, R. R., and M. K. Yau (1989) A short course in cloud physics, Butterworth-Heinemann, Woburn, Massachusetts.

Sherwood, S. C (1999), Convective Precursors and Predictability in the Tropical Western Pacific, *Mon. Wea. Rev.*, 127, 2977-2991.

Sherwood, S. C., P. Minnis, and M. McGill (2004), Deep convective cloud-top heights and their thermodynamic control during CRYSTAL-FACE, *J. Geophys. Res.*, 109, D20119, doi:10.1029/2004JD004811.

Stephens, G. L., et al. (2008), CloudSat mission: Performance and early science after the first year of operation, *J. Geophys. Res.*, 113, D00A18, doi:10.1029/2008JD009982.

684 Stevens, B. and G. Feingold (2009), Untangling aerosol effects on clouds and precipitation in a
685 buffered system, *Nature*, *461*, 607-613.

686

687 Stevens, B., and J.-L. Brenguier (2009), Cloud-controlling Factors: Low Clouds, in *Clouds in the*
688 *Perturbed Climate System*, p173-196, editors. J. Heintzenberg and R. J. Charlson, The MIT
689 Press, Cambridge, Massachusetts.

690

691 Takemi, T., O. Hirayama, and C. Liu (2004), Factors responsible for the vertical development of
692 tropical oceanic cumulus convection, *Geophys. Res. Lett.*, *31*, L11109,
693 doi:10.1029/2004GL020225.

694

695 Weisman, M., and R. Rotunno (2004), “A Theory for Strong Long-Lived Squall Lines” Revisted,
696 *J. Atmos. Sci.*, *61*, 361-382.

697

698 Winker, D. M., W. H. Hunt, and M. J. McGill (2007), Initial performance assessment of
699 CALIOP, *Geophys. Res. Lett.*, *34*, L19803, doi:10.1029/2007GL030135.

700

701 Wu, D. L., et al. (2008), Validation of the Aura MLS cloud ice water content measurements, *J.*
702 *Geophys. Res.*, *113*, D15S10, doi:10.1029/2007JD008931.

Table 1. CALIPSO centroid derivatives calculated using Equations (2) and (3). Calculations bin data according to the relative humidity at 925 hPa. Derivatives are in m per 0.1 AOD units.

		<u>1° x 1° AODs</u>		<u>3° x 3° AODs</u>	
	<u>Cloud occurrence centroids</u>	<u>Land</u>	<u>Ocean</u>	<u>Land</u>	<u>Ocean</u>
All cloud depths		20	143	15	30
Cloud depths > 1 km		28	173	26	48
Cloud depths > 2 km		58	174	53	85
	<u>Mass weighted centroids</u>	<u>Land</u>	<u>Ocean</u>	<u>Land</u>	<u>Ocean</u>
All cloud depths		36	167	34	43
Cloud depths > 1 km		26	59	26	58
Cloud depths > 2 km		26	54	26	55

718 Table 2. CALIPSO centroid derivatives calculated using Equations (2) and (3). Calculations bin
 719 data according to the relative humidity at 925 hPa and at 200 hPa. Derivatives are in m per 0.1
 720 AOD units. AODs are derived from 3° x 3° averages.

722	<u>Cloud occurrence centroids</u>	<u>Land</u>	<u>Ocean</u>
723	All cloud depths	33	50
724	Cloud depths > 1 km	44	51
725	Cloud depths > 2 km	65	75
726			
727	<u>Mass weighted centroids</u>	<u>Land</u>	<u>Ocean</u>
728	All cloud depths	49	66
729	Cloud depths > 1 km	54	60
730	Cloud depths > 2 km	59	62

732

733 Table 3. Z_c centroid derivatives for the four seasons over land and ocean. Values are for $3^\circ \times 3^\circ$
 734 AOD calculations. Derivatives are in m per 0.1 AOD increment units.

	<u>Original</u>		<u>Corrected</u>	
<u>Cloud occurrence centroids</u>	<u>Land</u>	<u>Ocean</u>	<u>Land</u>	<u>Ocean</u>
December-January-February	64	76	69	46
March-April-May	81	66	47	37
June-July-August	169	110	58	51
September-October-November	-35	69	-40	45

743
 744
 745
 746
 747

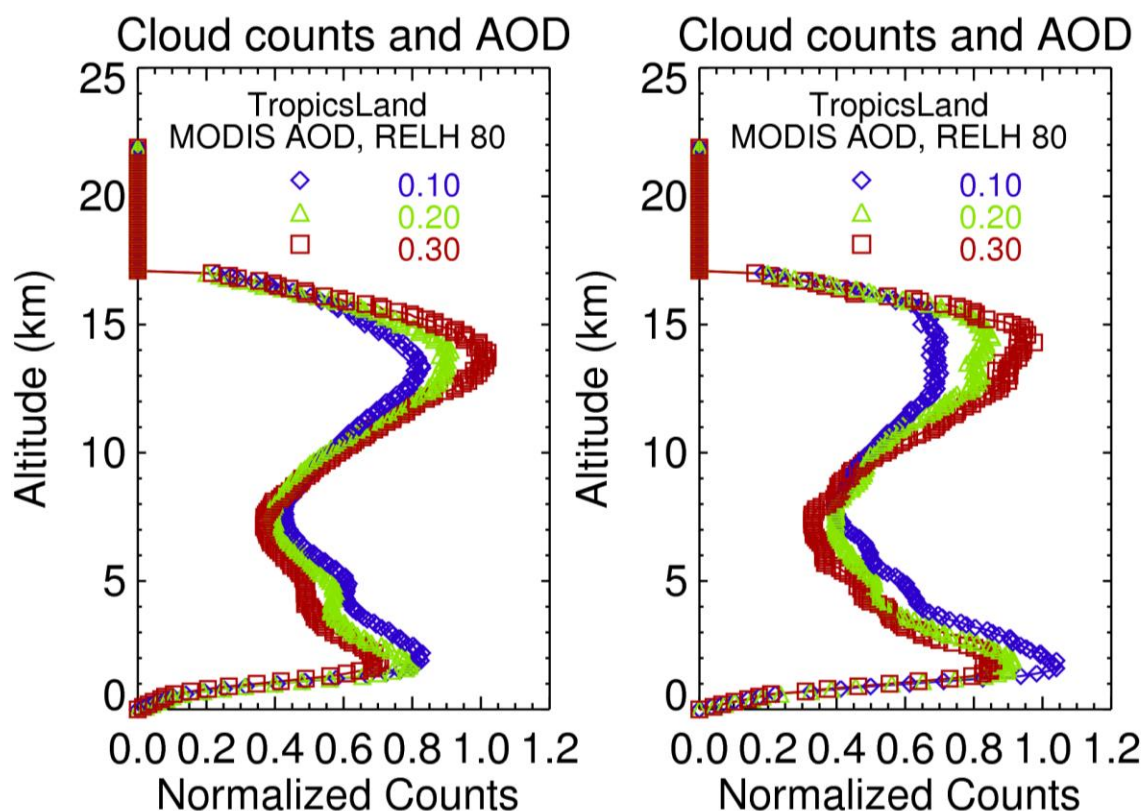
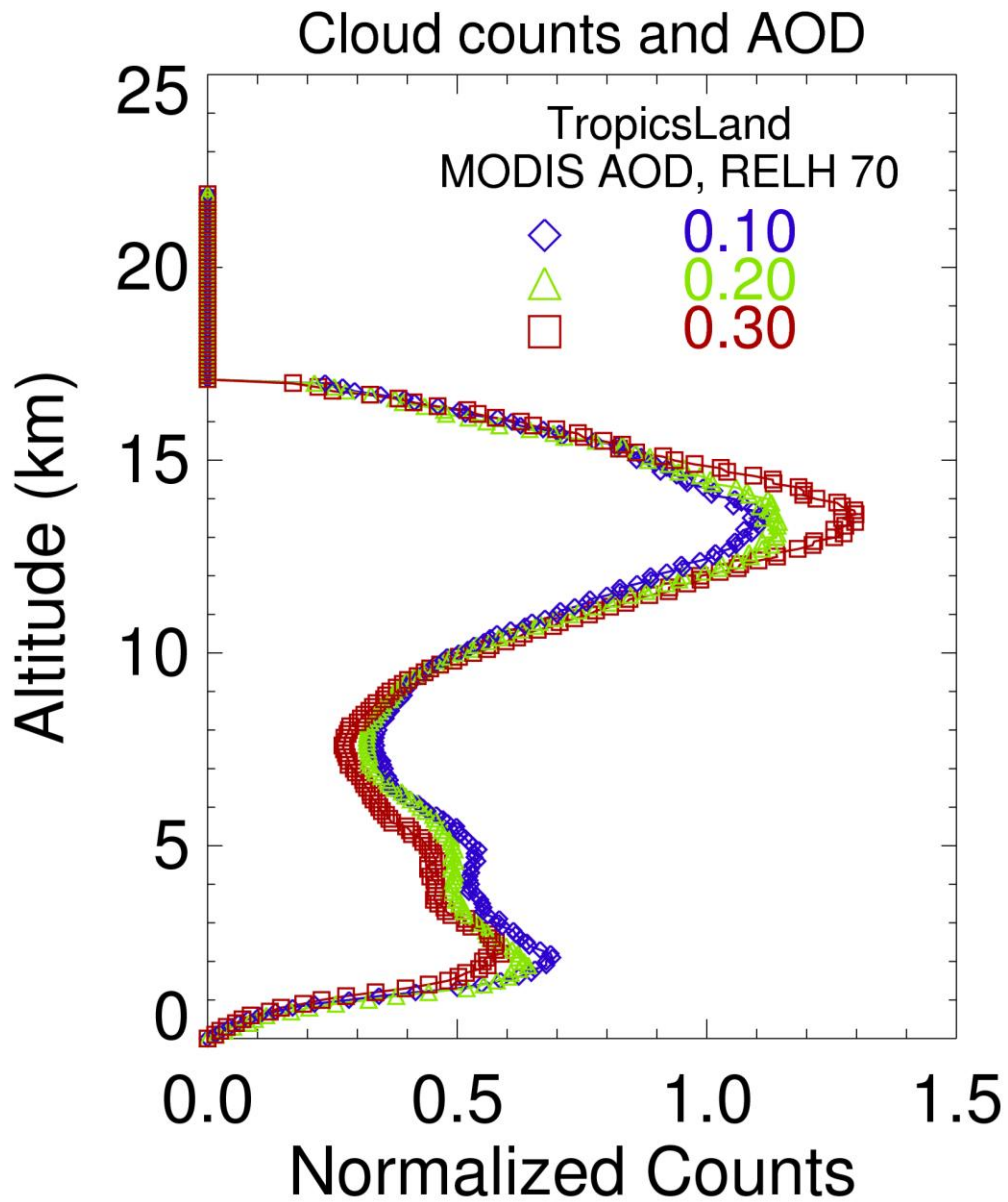


Figure 1. Left panel) Normalized cloud counts over the Tropics (20S – 20N) and land in 2008 for all months of the year and three bins of MODIS AODs (0.10 – 0.20, 0.20-0.30, 0.30-0.40), and AIRS relative humidity of 60-70% at 925 hPa. Right panel) Same as the left panel, except that AIRS relative humidity is 80-90% at 925 hPa. AODs and RL-GEOPROF data are from 1° x 1° degree latitude-longitude data bins.



755

756 Figure 2. Normalized cloud counts over the Tropics (20S – 20N) and land in 2008 for all

757 months of the year and three bins of MODIS AODs (0.10 – 0.20, 0.20-0.30, 0.30-0.40),

758 and AIRS relative humidity of 70-80% at 925 hPa and 60-90% at 200 hPa near 11 km

759 altitude.

760

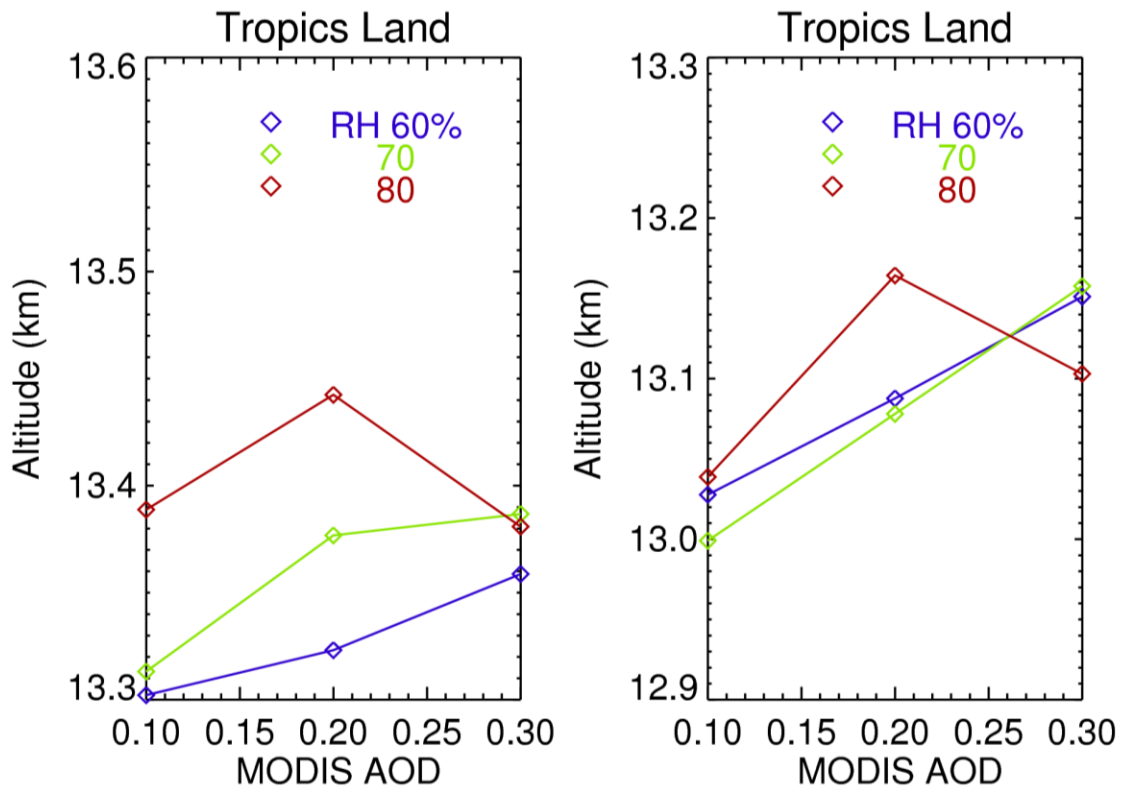


Figure 3. Left panel) Altitude centroids of cloud occurrence (see Equation 2) over the Tropics (20S – 20N) and land in 2008 for all months of the year for all cloud depths. Right panel) Same as the left panel except that only clouds with vertical depths greater than 2 km are included.

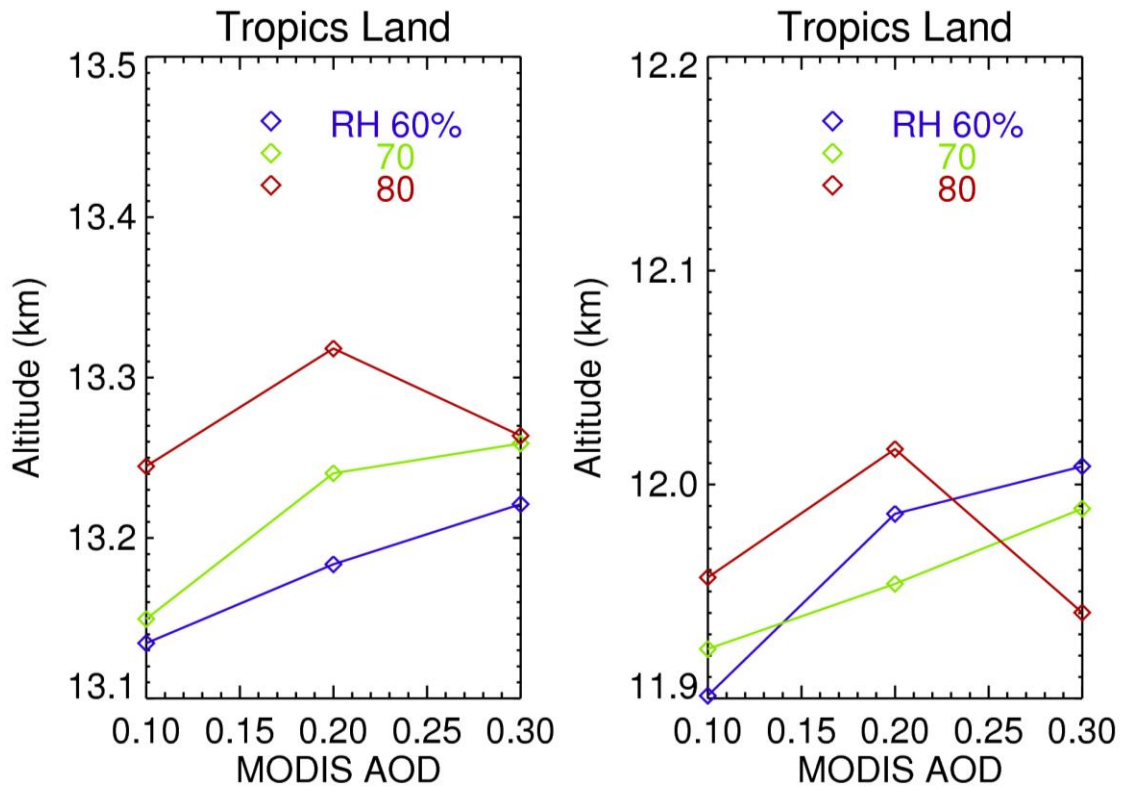


Figure 4. Left panel) Altitude centroids of mass weighted cloud occurrence (see Equation 3) over the Tropics (20S – 20N) and land in 2008 for all months of the year for all cloud depths. Right panel) Same as the left panel except that only clouds with depths greater than 2 km are included.

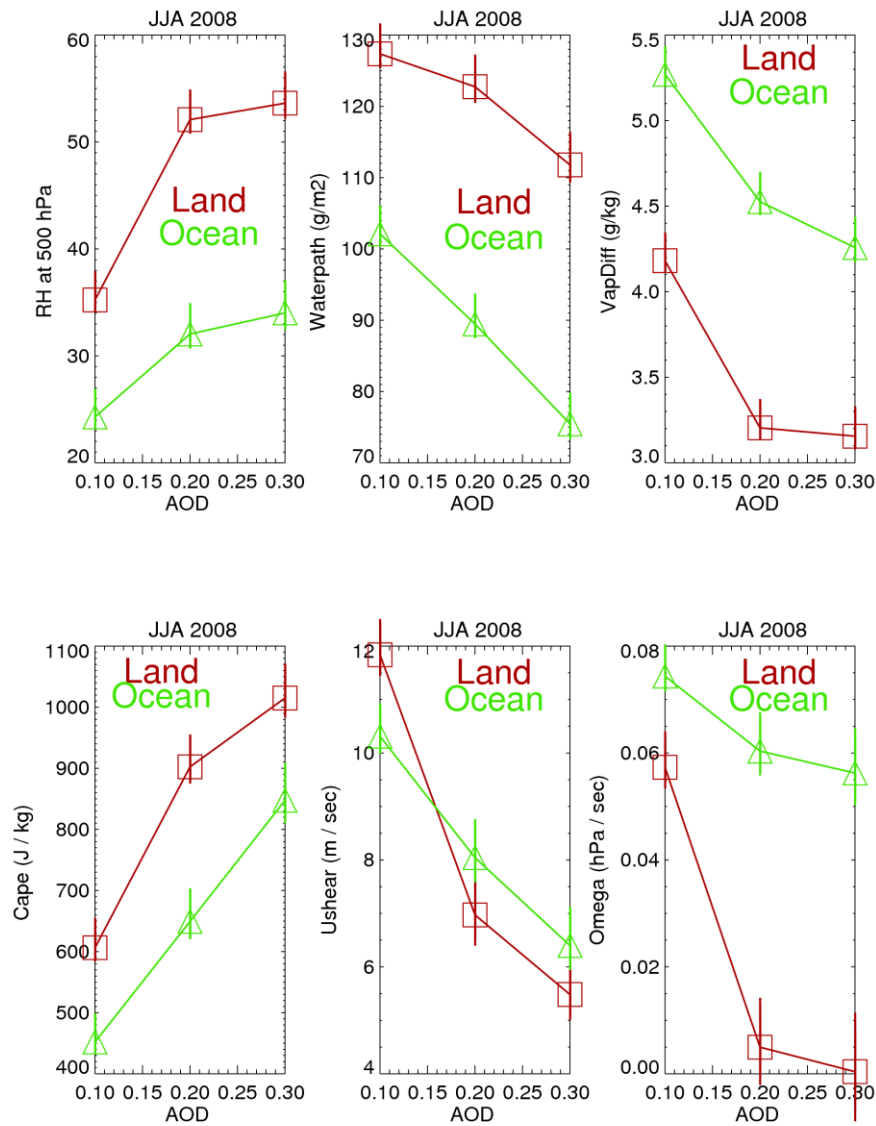


Figure 5. Variations of average MODIS AOD over land and ocean (Tropics 20S – 20 N) of AIRS relative humidity at 500 hPa, MODIS water paths (gm/m^2), vapor deficit (g/kg), FNL CAPE (J kg^{-1}), wind shear of the horizontal wind (m/sec), and omega (pressure tendency) (hPa/sec) in 2008 for June-July-August for cloud widths greater than 2 km. Note that positive omega values correspond to a downward vertical velocity. The vertical bars are the 95 confidence limits of the means.

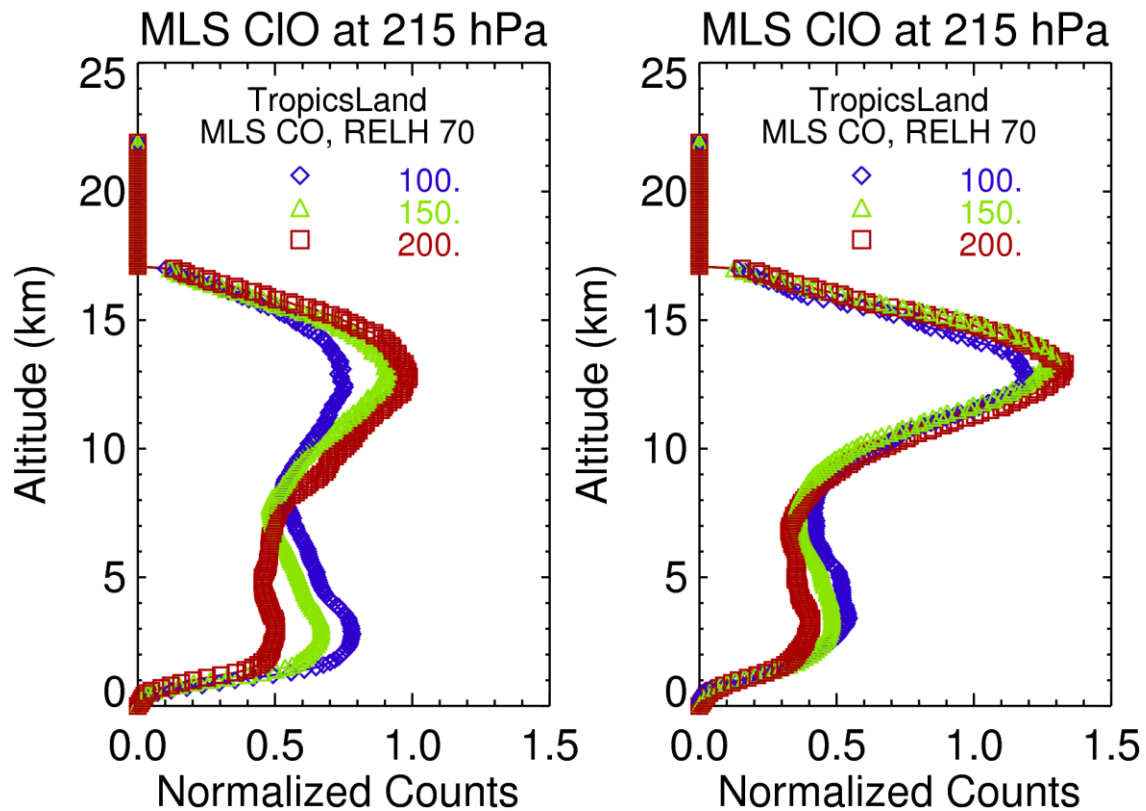
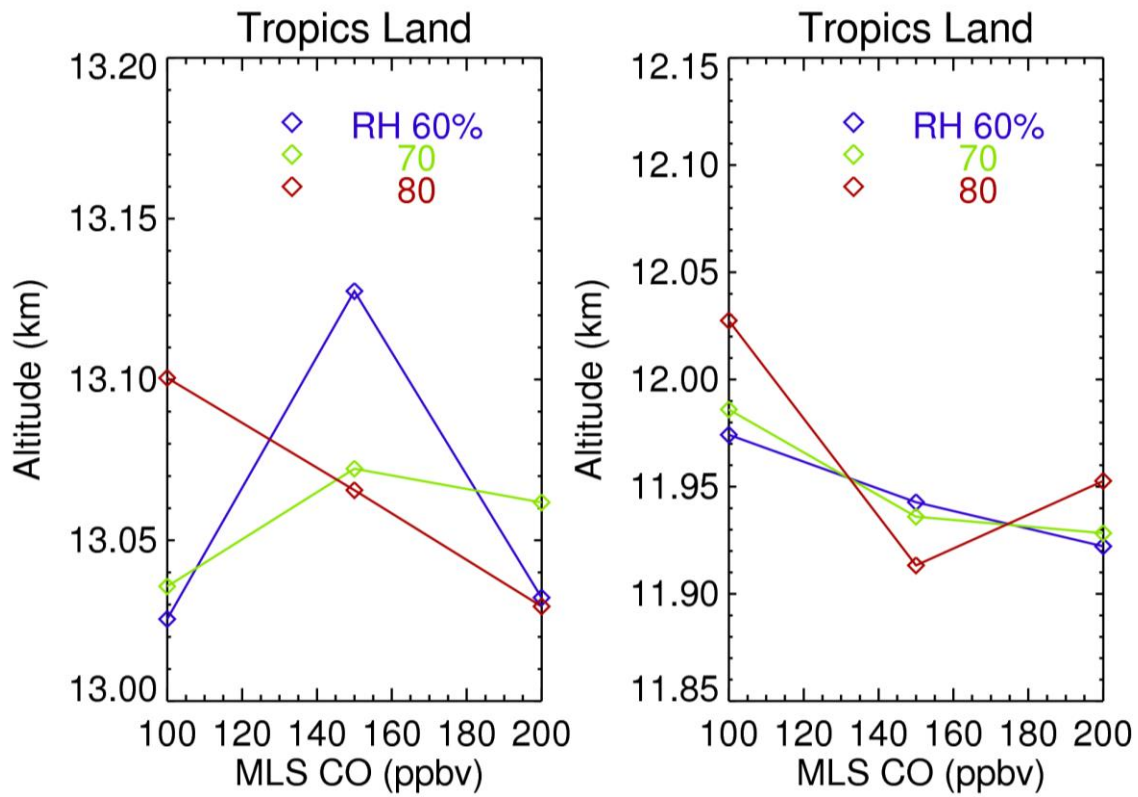


Figure 6. Left panel) Normalized cloud counts over the Tropics (20S – 20N) and land in 2008 for all months of the year and three bins of MLS CO (100 - 150, 150 - 200, and 200 – 250 ppbv) for cloud depths greater than 2 km, and AIRS relative humidity of 60-70% at 925 hPa. Right panel) Same as left panel, except that AIRS relative humidity is 60 to 90% at 200 hPa.



789

790

Figure 7. Left panel) Altitude centroids of cloud occurrence (see Equation 1) over the

791

Tropics (20S – 20N) and land in 2008 for all months of the year for cloud depths greater

792

than 2 km. Right panel) Same as the Left panel except for mass centroids (see Equation 3).